Structural Analysis of the Plasmodial Proteins ZNHIT3 and NUFIP1 Provides Insights into the Selectivity of a Conserved Interaction

Marie-Eve Chagot, Alexis Boutilliat, Alexandre Kriznik, Marc Quinternet

Structural Analysis of the Plasmodial Proteins ZNHIT3 and NUFIP1 Provides Insights into the Selectivity of a Conserved Interaction

Marie-Eve Chagot,[1] Alexis Boutilliat,[2] Alexandre Kriznik,[1,2] and Marc Quinternet *,[2]

Affiliations :

1. Université de Lorraine, CNRS, IMoPA, F-54000 Nancy, France

2. Université de Lorraine, CNRS, INSERM, IBSLor, F-54000 Nancy, France

*. Corresponding author

KEYWORDS

Malaria; ZNHIT3; NUFIP1; snoRNA; snoRNP; Ribophagy; Biophysics; Protein interaction; NMR; AlphaFold; Calorimetry; DLS; Molecular dynamics simulation; Druggability

ABSTRACT

Malaria is a widespread and lethal disease caused by the *Plasmodium* parasites that can infect human beings through Anopheles mosquitoes. For that reason, the biology of *Plasmodium* needs to be studied to develop antimalarial treatments. By determining the three- dimensional structures of macromolecules, structural biology helps to understand the function of proteins and can reveal how interactions occur between biological partners. Here, we studied the ZNHIT3 and NUFIP1 proteins from *Plasmodium* falciparum, two proteins tightly linked to the ribosome biology. Due to their important functions in post-translational modifications of ribosomal RNAs and in ribophagy, these proteins participate in the survival of cells. In this study, we solved the three-dimensional structure of a thermally stable and species-dependent complex between fragments of these proteins. Our results were compared to the AlphaFold predictions, which motivated the study of the free ZNHIT3 fragment that binds NUFIP1. We showed that the latter fragment multimerized in vitro but also had the inner ability to change its conformation to escape the solvent exposition of key hydrophobic residues involved in the interaction with NUFIP1. Our data could open the gate to selective drug discovery processes involving these two proteins.

INTRODUCTION

Malaria is one of the most widespread diseases, with an estimated 229 million cases worldwide in 2019, according to the World Health Organization. It is responsible for almost half a million deaths, more than 65% of which occur in children under 5 years of age. Malaria is primarily caused by two parasites, *Plasmodium* falciparum and *Plasmodium* vivax, that are disseminated to people through the bites of Anopheles mosquitoes. It represents a public health issue with approximately US$3 billion funded in 2019 for disease control and elimination. Thus, a better understanding of the biology of *Plasmodium* agents appears necessary for the development of effective treatments, especially to overpass emerging resistances to known antimalarial drugs. (1,2)

The *Plasmodium* parasite is a unicellular eukaryotic organism that uses vertebrates, such as humans, to replicate itself. Replication means fine regulations of many biological pathways and synthesis of new proteins. In this way, the ribosomal machinery plays a major role in the life cycle of the parasites. (3) Ribosomes are large ribonucleoproteins containing several ribosomal RNAs (rRNAs) and dozens of ribosomal proteins. The right functioning of the ribosome requires post-translational modifications of rRNAs such as 2′-O methylation or pseudo-uridylation. (4) Obviously, these modifications are not randomly distributed on rRNAs. Small nucleolar ribonucleoproteins (snoRNPs) are guided modifying systems that involve (i) a small nucleolar RNA (snoRNA) that specifically recognizes a modification spot on the rRNA and (ii) a set of four core proteins, including an enzyme able to catalyze the 2′- O methylation or pseudo-uridylation reactions on target nucleotides. (5) 2′-O methylation is performed by fibrillarin, with the help of S-adenosine methionine and SNU13, NOP56, and NOP58 proteins, whereas pseudo-uridylation is managed by dyskerin, with the help of NOP10, NH2, and GAR1 proteins. (6,7) In eukaryotes, unlike archaes, snoRNPs do not self-assemble, and their assembly needs to be assisted by protein factors that interact transiently in an ordered process that results in a functional particle. (8) Among these protein factors, we and others described the functional and structural features of Rsa1/NUFIP1, Hit1/ZNHIT3, Bcd1/ZNHIT6, or the R2TP complex. (9−20) We showed that some features, especially in terms of structures, are shared through species, and more precisely, we demonstrated that NUFIP1 (also known as Rsa1 in yeast) and ZNHIT3 (also known as Hit1 in yeast, or TRIP3 elsewhere) formed an interleaved complex that behaves as a unique protein chain. (13)

NUFIP1 is a platform protein that can recruit the core protein SNU13 via a conserved motif called PEP. (9) The PEP motif mainly consists of an α-helix of about 20 residues that bind to a groove located on SNU13. This interface is

placed opposite to the patch in SNU13 that can bind the snoRNA, making possible a complex involving both snoRNA and NUFIP1. ZNHIT3 contains at least two domains: a ZN-HIT domain that consists of a double zinc-finger, probably involved in protein−protein interaction, and a PAC-HIT domain that folds into a clamp able to trap an α-helix, here again of about 20 residues, located in the sequence of NUFIP1 (see Figure 1 for the organization of the protein domains in NUFIP1 and ZNHIT3). (10,13,14) Remarkably, the PAC-HIT domain in ZNHIT3 proteins contains hydrophobic residues that are protected from the aqueous solvent by NUFIP1.

In yeast and human cells, it was demonstrated that the ZNHIT3:NUFIP1 interaction was essential to stabilize the two proteins and maintained normal levels of snoRNAs as well as normal growth rates. (10) This complex was also pointed to be important in the ribophagy pathway. (21) Ribophagy consists of the lysosomal degradation of ribosomes and supplies nutrients to the cells under starvation stress. (22) Under this condition, ZNHIT3:NUFIP1 would associate with ribosomes and chaperons them to autophagosomes via the LC3B protein. Noticeably, a conflicting study, based on NUFIP1-depleted cells, suggests, however, that NUFIP1 would not influence the starvation-induced ribophagic flux. (23) Interestingly enough, the N-terminus of NUFIP1 still displays sequence conservation with LC3B-interacting regions (LIRs), whose consensus motif is [W/F/Y]xx[L/I/V]. (21) Typically, LIRs fold into a β-strand upon binding of LC3B to promote hydrophobic contacts within an intermolecular β-sheet. (24,25) This feature is in line with the platform role of NUFIP1.

The snoRNP assembly, the rRNA post-translational modification, and ribophagy processes are not still fully understood, especially in parasites, but are essential for cell survival. It was nonetheless demonstrated that an autophagy pathway can function in *P. falciparum*, under nutrient stress conditions, through a dozen of autophagy-related proteins (ATG), with a more specific involvement of ATG8 in ribophagy, the latter protein displaying structural similarities with LC3B. (26−28) Concerning rRNA modifications in the malaria parasites, to our knowledge, little is known, but we have noticed that directly involved proteins such as fibrillarin, dyskerin, and NOPs appear conserved in these organisms, suggesting a regulation mode similar to what is commonly observed in yeast or human cells. Moreover, the snoRNA landscape in *P. falciparum* could be analyzed and showed that snoRNAs were mainly present in a single copy, meaning that no rescue effect could be retrieved in the case of default in these snoRNAs. (29) Furthermore, plasmodial snoRNAs were found to be excreted from infected red blood cells in extracellular vesicles (EVs). In this form, their role was not formally identified, but their presence in EVs may be of importance for communication between parasites. In general, ribophagy and snoRNP formation remain under-studied in *Plasmodium* parasites, although they may represent important functions to target to affect the virulence of the pathogen. (27,28)

In this study, we identified ZNHIT3 and NUFIP1 from *P. falciparum* in protein databases, thanks to structural data and designed fragments in these proteins that can interact in vitro. We solved the three-dimensional (3D) structure of this complex, which folds into an interlacing pattern, characteristic of the ZNHIT3:NUFIP1 interaction. Importantly, we showed that this complex was highly stable to temperature and demonstrated that the formation of inter-species complexes between fragments of yeast, human, and plasmodial ZNHIT3 and NUFIP1 was not possible. Using biophysical and molecular dynamics (MD) approaches, we studied the isolated C-terminal domain of the plasmodial ZNHIT3 protein and demonstrated that this fragment, which can interact with NUFIP1, tended to multimerize but could potentially modify its fold to minimize the solvent exposition of key hydrophobic residues. Our experimental results are discussed in regard of the AlphaFold 3D structures, which remarkably predict the bound state of the two isolated proteins but also the complex they can form. Altogether, our study suggests that the ZNHIT3:NUFIP1 interaction, which occurs in cell survival and replication pathways, is species specific and could be considered, thanks to structural data, as a target of choice in druggability studies of plasmodial proteins.

MATERIALS AND METHODS

Protein Identification.

The protein sequences of ZNHIT3 and NUFIP1 from *P. falciparum* 3D7 (pf-ZNHIT3 and pf-NUFIP1) were retrieved from the UniProt and NCBI databases according to their putative names. (30) Along the article, ZNHIT3 and NUFIP1 proteins from *P. falciparum* and *Homo sapiens* are designated with the prefixes “pf-” and “hs-”, respectively. ZNHIT3 and NUFIP1 proteins from *Saccharomyces cerevisiae* are designated as Hit1 and Rsa1, respectively.

Protein Expression and Purification.

The protocols used in this study were previously described. 10,13,31 Briefly, the protein fragments containing an N-terminal 6xHIS tag followed by a cleavage site for the 3C PreScission protease were encoded on a pnEA-3CH vector providing resistance to ampicillin. (31) The additional sequence provided by the plasmid is as follows: MGSSHHHHHHSSGTGSGLEVLFQ/GPH. The protein fragments that did not contain additional purification tags were encoded on pnYK or pnCS vectors, providing resistances to kanamycin and spectinomycin, respectively. For individual expression of protein fragments, Ca 2+ -competent E. coli BL21(DE3) bacteria were transformed with a pnEA-3CH vector. For protein complexes, this time bacteria were co-transformed with two plasmids, one of the two partners being encoded on a pnEA-3CH vector, the other one being encoded on a pnYK or pnCS vector. Using these combinations of vectors permits us to produce similar amounts of each of the two protein partners in bacteria. The same methods were applied for the free proteins and complexes. Positive clones, selected on LB-agar plates, were grown in liquid media at 37 °C until absorbance at 600 nm reached 0.6. The overexpression of proteins was triggered with 0.2 mM IPTG (isopropyl β- D -1-thiogalactopyranoside), and cultures were done at 20 °C for 16 h. LB, 15 N-enriched M9, and 13 C/15 N-enriched M9 media supplemented with selective antibiotics were used. After resuspension of the cell pellet in a

lysis buffer (25 mM HEPES, 300 mM NaCl, 10 mM imidazole, 0.5 mM TCEP, pH 7.5) and sonication, the soluble fraction was put on TALON beads. Elution was performed, either with a specific cleavage using the 3C PreScission protease or with a lysis buffer supplemented with 300 mM imidazole. If required, a final size-exclusion chromatography step in 10 mM NaPi, 150 mM NaCl (pH 6.4) permitted us to isolate the protein fractions of interest. The purification process was analyzed using sodium dodecyl sulfate (SDS)− polyacrylamide gel electrophoresis (PAGE) and Coomassie blue staining.

Nuclear Magnetic Resonance and Structure Calculation.
Usual homo- and hetero-nuclear two-dimensional (2D) and 3D nuclear magnetic resonance (NMR) spectra were recorded at 293 K on a 13 C/ 15 N labeled sample of the pf-ZNHIT3(265-332):pf-NUFIP1(817-841) complex concentrated at 0.7 mM in 10 mM NaPi, 150 mM NaCl (pH 6.4) using a 600 MHz spectrometer equipped with a TCI cryoprobe (Bruker). Assignment of the NMR frequencies was performed with CARA. (32) Backbone resonances were turned into dihedral restraints, thanks to TALOS-N. (33) Inter- proton distances were derived from 2D 1 H− 1 H NOESY and 3D 1 H− 13 C and 1 H− 15 N NOESYHSQC spectra recorded with a mixing time of 120 ms. CYANA 3.98.13 was used to iteratively assign and quantify NOE cross-peaks. (34) The final CYANA and TALOS-N restraints were used to calculate 100 structures that were water-refined with AMBER 14. (35) The 20 AMBER structures with the lowest restraint energies were kept in a final representative bunch. The 3D structures were drawn and analyzed with PyMOL. (36)

Differential Scanning Calorimetry.
Differential scanning calorimetry (DSC) experiments were performed on a Microcal VP-DSC apparatus equipped with 0.54 mL cells, at a pressure of 2 atm. The thermograms were recorded using a protein complex concentration of around 35 μM into 10 mM NaPi, 150 mM NaCl (pH 6.4). A scanning window from 25 to 125 °C with a constant scan rate of 1 °C/min was applied. Origin 7.0 software was used to determine T m (midpoint of the unfolding transition). Baselines recorded with both cells filled with buffer were subtracted from the experimental traces to obtain the heat capacity curves (ΔCp , excess heat capacity, vs temperature).

Dynamic Light Scattering.
Dynamic light scattering (DLS) experiments were performed at 20 °C in 10 mM NaPi, 150 mM NaCl (pH 6.4) using a Zetasizer Nano ZS instrument (Malvern Panalytical) in a small-volume quartz cell. Data were processed with the Zetasizer software (Malvern) with default parameters.

Isothermal Titration Calorimetry.
The isothermal titration calorimetry (ITC) experiment was performed using a VP-ITC (Malvern, UK), the temperature being set to 20 °C. The protein, concentrated at 70 μM in 10 mM NaPi, 150 mM NaCl (pH 6.4), was repeatedly injected into the mixing cell that contained buffer. Dissociation data were analyzed using the Origin software. The maximal critical transition concentration (CTC), corresponding to the dissociation constant of multimers, was calculated with a first derivative test. (37,38)

MD Simulation.
The best NMR structure of the pf-ZNHIT3(265-332):pf-NUFIP1(817-841) complex and of the structure of pf-ZNHIT3(265-332) predicted by AlphaFold were used as starting points for MD simulations. Calculations were performed in an explicit water solvent as previously described. (39) Briefly, the 3D structures were placed in a water cubic box (edge 60 Å), in the presence of 150 mM NaCl. The systems were prepared and analyzed with VMD. (40) The trajectories, generated with the NAMD-2.15 package, (41) were carried out in the isobaric−isothermal ensemble, at 300 K under 1 atm using, respectively, Langevin dynamics (damping coefficient 1 ps −1) and the Langevin piston method. Water and ions were first thermalized during 5 ns while restraining harmonically the backbone atoms of the proteins to their initial positions. Next, all positional restraints were removed, and the systems were thermalized under this condition for 15 ns.

RESULTS
ZNHIT3 and NUFIP1 Proteins from P. falciparum.
Looking for the ZNHIT3 and NUFIP1 proteins from *P. falciparum* (hereafter designated with the prefix “pf-”), we screened the Uniprot and NCBI databases. Concerning the 3D7 strain, we found entries that were unreviewed and described hypothetical proteins (Uniprot-Q8IK99 and NCBI- XP_001348881.1 for pf-NUFIP1; Uniprot-Q8I2Y4 and NCBI- PFI0825w for pf-ZNHIT3). We benefited from the AlphaFold predictions implemented in Uniprot and checked whether folded regions exhibiting good confidence scores (i.e., pLDDT > 90) in these putative proteins could match with the known 3D structures of their yeast and human homologues. (42)
For pf-ZNHIT3, we found two regions (120−156 and 267− 331) that nicely match, respectively, with the ZN-HIT and PAC-HIT domains of Hit1 and hs-ZNHIT3 (yeast and human proteins, respectively) (Figure 1A,B). For pf-NUFIP1, we found two regions, consisting of isolated α-helices whose structures and sequences match with the α-helices able to interact with SNU13, on the one hand, and with ZNHIT3, on the other hand, in yeast and human proteomes (Figure

1C,D). These are segments 683−711 and 813−836, respectively. Moreover, using the iLIR autophagy database, (43) we also found putative LIR motifs in the pf-NUFIP1 sequence with a PSSM score ≥ 5.
This structural evidence strongly suggests that the proteins under the access codes Uniprot-Q8IK99 and Uniprot-Q8I2Y4 correspond to pf-NUFIP1 and pf-ZNHIT3, respectively. To confirm this conclusion, we sought to verify whether these proteins could directly interact to form a complex.

Design of a Soluble Complex between Plasmodial ZNHIT3 and NUFIP1 Proteins.
With 852 and 366 residues, respectively, plasmodial NUFIP1 and ZNHIT3 proteins detected in Uniprot are long proteins, mostly disordered concerning pf-NUFIP1, which may therefore be difficult to manipulate in their full-length version. Based on careful analyses of the protein sequences, known 3D structures of yeast and human homologues, and 3D predictions coming from AlphaFold, we designed fragments of pf-ZNHIT3 and pf-NUFIP1 that should have the intrinsic ability to form a stable and soluble protein complex in vitro.
Thus, we encoded the fragments 265−332 of pf-ZNHIT3 and 817−841 of pf-NUFIP1 on expression plasmids and performed a co-expression assay in a E. coli BL21(DE3) strain. Remarkably, co-expression permitted to clearly observe the two fragments on SDS−PAGE (Figure 2). The gel filtration profile revealed that the two proteins co-eluted in fractions, with an elution volume compatible on our purification automat with a single heterodimer of ∼13 kDa (Figure 2). Thus, this demonstrates that the pf-NUFIP1 and pf-ZNHIT3 proteins behind the Uniprot-Q8IK99 and Uniprot-Q8I2Y4 entries are no longer hypothetical and allows us to consider a structural study of their interaction in solutions using NMR.

NMR Structure of the Complex between Pf-ZNHIT3 and Pf-NUFIP1 Proteins.
The pf-ZNHIT3(265-332):pf- NUFIP1(817-841) complex was ^{13}C- and ^{15}N-labeled, thanks to the bacterial recombinant expression in minimal medium enriched with 15 NH 4 Cl and 13 C-d6-glucose. We first assigned the large majority of the 1 H, 13 C, and 15 N resonances to get the 3D structure of the complex. At last, we obtained a well- defined bunch of 20 water-refined structures using inter-proton distance and dihedral angle restraints (Figure 3A, Table 1). In our experimental structure, pf-ZNHIT3(265−332) folds into a PAC-HIT domain whose five α-helices form a jaw that bites pf-NUFIP1(817−841), the latter being mainly folded into a α-helix. The complex is efficiently stabilized by strong hydrophobic forces resulting from numerous hydrophobic side chains that point to the core of the structure (Figure 3B). Indeed, nearly one out of four residues in the overall sequence of the complex is a hydrophobic residue located at the interface between the two protein fragments. Thus, the plasmodial complex is typical of the ZNHIT3:NUFIP1 interaction already observed with yeast and human proteins (Figure 3C). The root mean square deviations (rmsds) measured with the TM-align server (44) are 2.01 and 2.38 Å in regard of the human and yeast complexes. As observed for hs-ZNHIT3(85−155), pf- ZNHIT3(265−332) displays less loop regions than Hit1(70−164). Concerning pf-NUFIP1(817−841), it super- imposes well with hs-NUFIP1(462−495) and Rsa1(317− 352). Whereas the C-terminal part of Rsa1(317−352) forms a second α-helix that contacts Hit1(70−164), hs-NUFIP1(462− 495) is mainly disordered in the corresponding region (Figure 3C). The fragment selected for the plasmodial pf-NUFIP1 is significantly shorter than the ones used to determine the 3D structures of the yeast and human complexes. It contains, in a C-terminal loop, two phenylalanine residues (F837 and F838) that bind a hydrophobic pocket located on the side of pf-ZNHIT3(265−332) (Figure 3B). This appeared sufficient to stabilize the C-terminus end of pf-NUFIP1(817−841).

AlphaFold Predictions Agree with the Experimental Structures of Plasmodial ZNHIT3 and NUFIP1.
Remarkably, our experimental structure of pf-ZNHIT3(265−332):pf- NUFIP1(817−841) aligns well with the predictions made by AlphaFold on the isolated protein domains (Figure 4A,B). Cα rmsds are, respectively, 0.66 and 0.79 Å between the predicted and the experimental structures of pf-ZNHIT3(265−332) and pf-NUFIP1(817−841). Moreover, using heavy atoms, the corresponding rmsd values are 0.75 and 0.96 Å, demonstrating that even the positioning of the side chains is very similar in the experimental and predicted structures. For example, the positions of the two phenylalanine residues, F837 and F838 in pf-NUFIP1, are in phase between both the AlphaFold and NMR structures, demonstrating that these residues are ready to interact with their binding pocket in pf-ZNHIT3.
We benefited from the open-access server ColabFold (https://colab.research.google.com/github/sokrypton/ColabFold/blob/main/AlphaFold2.ipynb) to test if AlphaFold could also precisely predict the 3D structure of the plasmodial complex. Remarkably, despite a noticeable deviation in the position of the first three N-terminal residues in pf- NUFIP1(817−841), the results coming from ab initio prediction align well with the 3D structure that we experimentally determined by NMR spectroscopy (Figure 4C). As evidence, Cα and heavy atom rmsd values between AlphaFold are, respectively, 0.63 and 0.82 Å. Thus, the position of the side chains, especially in the hydrophobic interfacing residues, convincingly matches in the two structures.

Proteins from P. falciparum Display a High Thermal Stability.
To go further in the biophysics of the ZNHIT3:NUFIP1 interaction, we tested the thermal stability of this association using scanning calorimetry (DSC) recorded at a pressure of 2 atm (which prevents boiling of the aqueous buffer) and obtained denaturation temperatures of 71.8, 78.3, and 90.0 °C for the human, yeast, and plasmodial complexes, respectively (Figure 5A). Thus, we measured a higher thermal stability for the plasmodial complex. Moreover, human and yeast complexes tended to precipitate upon the increase in the temperature (as demonstrated by the sharp drop in the signal). In contrary, the plasmodial proteins remained safe all along the experiment. Interestingly, no steps were

observed within this curve, meaning that the dissociation of the two partners could not be distinguished from the denaturation process of each protein. To complete DSC data, we gently heated the protein complex samples at 98 °C, under atmospheric pressure, in a dry water-bath using six temperature steps of 10 min (20, 35, 50, 65, 80, and 98 °C) and then left the samples to cool at 20 °C. In agreement with the DSC results, the yeast and human complexes started to precipitate at temperatures between 65 and 80 °C, whereas the plasmodial sample remained clear (Figure 5B). Remarkably, the 1 H− 15 N HSQC and 1 H− 13 C METHYL-SOFAST HMQC NMR spectra of pf-ZNHIT3(265−332):pf-NUFIP1(817−841) recorded at 20 °C were not affected in terms of peak position and intensity after the heating/cooling cycle, although the denaturation temperature of the complex was exceeded by 8 °C (Figure 5C). This demonstrates that the initial interleaved conformation of the complex is recovered after the temperature returns to a low value.

ZNHIT3:NUFIP1 Interaction Is Species-Specific.

Next, to assess the specificity of the ZNHIT3:NUFIP1 interaction, we tested whether we could reconstitute complexes between ZNHIT3 and NUFIP1 protein fragments coming from different species. To test this, we performed protein co-expression assays in E. coli (Figure 6A). Interestingly, no soluble complex between pf-ZNHIT3(265−332) and Rsa1(317−352) or hs-NUFIP1(462−495) could be recon- stituted in bacteria and eluted from TALON beads, meaning that the pf-NUFIP1(817−841) fragment could not be substituted by its yeast and human homologues. Positive control experiments showed that the intra-species complexes were well formed in the bacteria, whereas nonspecific binding to TALON beads was not detected with untagged hs-NUFIP1 and Rsa1 fragments.

We had previously observed this behavior by failing to form inter-species complexes between yeast Hit1 and hs-NUFIP1. (13) One explanation can be provided by observing the 3D structures of the ZNHIT3:NUFIP1 complexes. Indeed, we could highlight several steric clashes that would occur if yeast and human NUFIP1 were trapped in the plasmodial ZNHIT3 (Figure 6B). Based on this observation, we aimed to define a rule in the amino acid sequence of the ZNHIT3 and NUFIP1 proteins that could drive the intra-species specificity of the interaction. With help of the mTM-align server, (45) we reported the steric clashes highlighted in Figure 6B on a multiple sequence alignment extracted from a structural superimposition of the plasmodial, yeast, and human ZNHIT3:NUFIP1 complexes (Figure 6C). We first noticed that the similarity and the identity are low on this type of alignment when the three ZNHIT3 and NUFIP1 domains are considered, although the complexes display close 3D folds. Even if residues L277, M326, and I329 in pf-ZNHIT3 display similarities with corresponding hs-ZNHIT3 and Hit1 amino acids, the facing residues in hs-NUFIP1 and Rsa1 that promote steric clashes did not appear to be conserved, in terms of both spatial position and chemical properties. The same observation could be done with non- conserved residues K278, K297, and F299 in pf-ZNHIT3 and facing residues in hs-NUFIP1 and Rsa1. Remarkably, using molecular surface representation of the ZNHIT3:Hit1 protein structures extracted from *P. falciparum*, H. *sapiens*, and S. *cerevisiae* complexes, we observed that access to the core cavity that hosts NUFIP1 was quite different despite the similar hydrophobic propensity of this specific binding pocket (Figure 6D). In this context, it appeared difficult to highlight the clear protein sequence determinants that drive the specificity of the interaction. This is in agreement with what we had previously observed by comparing the yeast and human complexes and reinforces the idea that it is more the structures in their entirety, especially for the ZNHIT3 jaw, that confer the specificity than a few conserved positions. (13) Trivially, it could be represented as a kind of building block set in which the two partners from the same species assemble specifically but have incompatible indentations for the bricks of other species. In the end, the final assemblies result nonetheless in a similar architecture, whatever the species of interest.

Another hypothesis explaining the intra-species specificity is that the free pf-ZNHIT3 adopts an alternative conformation that is not able to bind NUFIP1 fragments. Interestingly, in our inter-species co-expression assays, we were able to recover soluble and significant amount of pf-ZNHIT3 after elution from TALON beads. We thus wondered if isolated recombinant plasmodial fragments could be purified individually.

Free Recombinant Pf-ZNHIT3(265−332) and Pf-NUFIP1(817−841) Are Difficult to Handle In Vitro.

In agreement with the protecting role described for ZNHIT3, we did not observe recombinant his-tagged pf-NUFIP1(817−841) that degrades quickly in bacteria (Figure 7A). On the contrary, after affinity and size-exclusion chromatography steps, we isolated soluble his-tagged pf-ZNHIT3(265−332) (Figure 7B). This appeared surprising due to the inner hydrophobicity of this protein fragment, especially for the interface with pf- NUFIP1. Further DLS experiments showed that the free his- tagged pf-ZNHIT3(265−332) displayed a mean size of 5.4 ± 0.6 nm, 30% bigger than the pf-NUFIP1-bound form, for which a mean size of 4.1 ± 0.7 nm was measured (Figure 7C). This suggests that the free protein fragment mainly formed small multimers in the solution, probably dimers. We used NMR to get more structural details on the sample, but unfortunately, a probably unfavorable exchange regime produced a very low-quality 1 H− 15 N HSQC spectrum, on which only few unfolded regions seem visible (Figure 7D). Increasing or decreasing the salt concentration and the pH, changing the buffer type, or cutting the 6xHIS-tag did not modify the behavior of pf-ZNHIT3(265−332). Using ITC, we monitored the behavior of the multimers upon dilution and observed low-value enthalpic signals that correspond to a dissociation process (Figure 7E). This low signal intensity suggests that the interactions that are broken upon dissociation are weak, which could correspond to the rupture of van der Waals forces. From these data, we derived a maximal CTC of 0.5 μM. It means that only a sub-micromolar concentration, not in agreement with our biophysical approaches, would permit us to study the monomeric form of pf-ZNHIT3(265− 332).

MD Simulation Favors a Close Conformation of the Free Pf-ZNHIT3(265−332).

The experimental data obtained on the free pf-ZNHIT3(265−332) led us to test the stability of the 3D structure predicted by AlphaFold, in which the hydrophobic residues interfacing with pf-NUFIP1 appear surprisingly well solvent-exposed. Indeed, we were impressed by the faculty of AlphaFold to predict an accurate 3D structure (Figure 4) almost independently of the chemical properties of the amino acids in the core of this protein domain. Starting from this prediction, we computed a short MD simulation and compared it with another simulation calculated with the NMR structure of pf-ZNHIT3(265−332) as the initial structure.

Interestingly, although starting from similar 3D structures of pf-ZNHIT3(265−332), the simulated behaviors of this domain totally differ whether the pf-NUFIP1(817−841) fragment is present or not (Figure 8, Supporting Information, Movie M1). For the first 5 ns of the simulation time, the position of backbone atoms being restrained, no structural differences were observed between the bound and free states of pf-ZNHIT3(265−332). At this stage, for the two simulations, the backbone rmsd values measured against the starting 3D structures remained low and stable over time. Strikingly, once the restraints were removed, the jaw of pf-ZNHIT3(265− 332), in the absence of pf-NUFIP1, immediately closed on itself, leading to drastic structural changes (Figure 8A). In comparison, the pf-NUFIP1-bound form of pf-ZNHIT3 remained stable all along the rest of the simulation time. To better illustrate this phenomenon (noticeable in the Supporting Information, Movie M1, and in the evolution of backbone rmsd values in Figure 8A), we followed distances between Cα atoms of residues I306 and I329 and of residues K274 and T300 over time and showed, with huge decrease in the mean distances (more than 6.5 Å), that the lower and upper lips of pf-ZNHIT3(265−332) pinch in the absence of pf-NUFIP1 (Figure 8B). Because of these structural changes, hydrophobic residues in pf-ZNHIT3(265−332) are less solvent-exposed, which should promote solubility in an aqueous medium. However, a side effect of this conformational change is a clear loss of accessibility of the pf-NUFIP1 binding site in pf- ZNHIT3. We would have liked to test this close state in a protein pulldown assay in which our two plasmodial fragments would have been purified individually and then mixed. However, multimerization of pf-ZNHIT3(265−332) and quick degradation of the recombinant pf-NUFIP1 fragment did not allow us to perform such an experiment.

Obviously, we have no experimental clue to claim that the pinched conformation of pf-ZNHIT3(265−332) is a realistic view of the free recombinant fragment or of the free protein in its cellular context. It could be the conformation assumed at sub- micromolar concentrations, where the multimers should dissociate, multimers being the juxtaposition of protein fragments in this conformation. Even if we discard the later hypothesis, MD renders here what was intuited by observing the pf-NUFIP1-bound structure of this fragment, meaning that the hydrophobic residues in the core of the open state of pf- ZNHIT3(265−332) seek protection from the solvent.

DISCUSSION

Druggability of the ZNHIT3:NUFIP1 Complex.

In this study, we have identified ZNHIT3 and NUFIP1 proteins from *P. falciparum* and present the structure and thermal stability of a minimal complex. Interestingly, these two proteins are conserved among eukaryotic organisms and form an interleaved complex that possesses structural properties that prevent the formation of inter-species complexes. Thus, the 3D complementarity between ZNHIT3 and NUFIP1 appears to be strictly restricted to a specie. This feature could be of importance in drug design studies because acting on the plasmodial interaction would not interfere with the interaction occurring in the human proteome.

In agreement with what was observed in yeast and human proteins, pf-ZNHIT3 seems to protect pf-NUFIP1 from degradation. Obviously, additional experimental efforts should be made to analyze the role of the plasmodial ZNHIT3:NUFIP1 interaction in vivo and study its involvement in snoRNP assembly and/or ribophagy. However, our DSC results tend to demonstrate that the ZNHIT3:NUFIP1 complex has been optimized during evolution to form a highly stable interaction, far more stable than the yeast or human interaction. The question is why. We could assume that the optimization of the interaction energy through a highly specific structural complementarity is a good means to prevent dissociation and flexibility of the complex, while the two partners have to execute their biological function together. We know that snoRNAs are mainly present in a single copy in the genome of *P. falciparum* and that rescue systems are absent from the parasite. (29) Thus, it appears likely that proteins involved in the snoRNP maturation and ribophagy pathways, such as ZNHIT3 and NUFIP1, were first optimized to avoid downstream defaults in these processes. This might compensate to some extent for the lack of snoRNA rescue systems. Measuring the thermal stability of other snoRNP assembly or core factors and ATG protein coming from *P. falciparum* could flesh out this hypothesis. If this hypothesis is confirmed, it suggests that destabilizing interactions between these proteins involved in the ribosomal machinery would likely decrease the growth of *Plasmodium* parasites and, by extension, the virulence of this and other eukaryotic pathogens.

AlphaFold Predicts the NUFIP1-Bound State of ZNHIT3 Proteins.

The knowledge of the 3D structure of the protein targets is crucial for screening putative ligands using in silico methods. The multitude of AlphaFold predictions available in databases is a chance for the design of new therapeutic inhibitors that would lock or prevent specific protein−protein interactions. Here, we obtained impressive superimposition results between the NMR structure of pf-ZNHIT3 bound to pf-NUFIP1 and the AlphaFold predictions of the individual partners. For this case, this teaches us that AlphaFold can remarkably predict protein structures in a ready-to-interact state and that it does not consider the solvent exposition of hydrophobic residues to accurately predict this state. However, these predictions make sense almost only if we have previous or experimental data validating the

interaction. Indeed, we showed, using MD simulation, that the fold predicted for pf-ZNHIT3(265−332) was susceptible to change in the absence of its partner. We do not know if the pinched conformation we obtained for this fragment is realistic or not. However, here, with in silico methods commonly used in computational screening, we showed that the access to the interaction site for pf-NUFIP1 in the core of pf-ZNHIT3 could be easily blocked. Thus, if no experimental data indicate that this major interface should be considered in a screening process, it could be discarded as a mistake. Interestingly, in the AlphaFold database, all the predicted ZNHIT3 proteins display an open state, ready to accommodate the corresponding NUFIP1 proteins. This and our previous studies teach us that this state should be the one to consider for drug design studies based on structural data. Finally, we also demonstrated that the plasmodial complex could be impressively modelized with AlphaFold despite the interleaved mode of interaction between the two partners. This permits us to state that all the ZNHIT3:NUFIP1 complexes, whatever the species, could be now predicted with trust with ab initio approaches. In our opinion, this is an important starting point for a better comprehension of the biological mechanisms involving these two proteins. Moreover, a deep structural and phylogenetic study that would engage dozens of predicted complexes could reaffirm the hypothesis we have raised about the specificity of the interaction, which would be driven primarily by the 3D structure of each partner rather by peculiar, conserved points in the amino acid sequences.

ASSOCIATED CONTENT

Supporting Information

*

The Supporting Information is available free of charge at https://pubs.acs.org/doi/10.1021/acs.biochem.1c00792.
Movie of a 20 ns MD simulation performed with pf- ZNHIT3(265−332) bound or not to pf-NUFIP1(817− 841) (MPG)

Accession Codes

The NMR structure and the 1 H, 13 C, and 15 N chemical shifts of pf-ZNHIT3(265−332):pf-NUFIP1(817−841) were, re- spectively, deposited in the Protein Data Dank and in the Biological Magnetic Resonance Bank under access codes 7QDW and 34693, respectively. Uniprot accession used for the plasmodial, human, and yeast ZNHIT3 (Hit1)/NUFIP1 (Rsa1) proteins are, respectively, Q8I2Y4/Q8IK99, Q15649/ Q9UHK0, and P46973/Q08932.

ACKNOWLEDGMENTS

This work was supported by the French National Center for Scientific Research (CNRS), University of Lorraine (France); the French National Research Agency (grant nos ANR-11- BSV8-01503 and ANR-16-CE11-0032-02); and SAYENS (Société d'Accélération du Transfert de Technologies, Technology Transfer Acceleration Corporation, Dijon, France). Access to the NMR, DSC, and DLS core facilities of the Biophysics and Structural Biology Department of UMS2008/US40 IBSLor is deeply appreciated (https:// umsibslor.univ-lorraine.fr/). We thank the EXPLOR core facility of the University of Lorraine for access to the calculation center (https://explor.univ-lorraine.fr/).

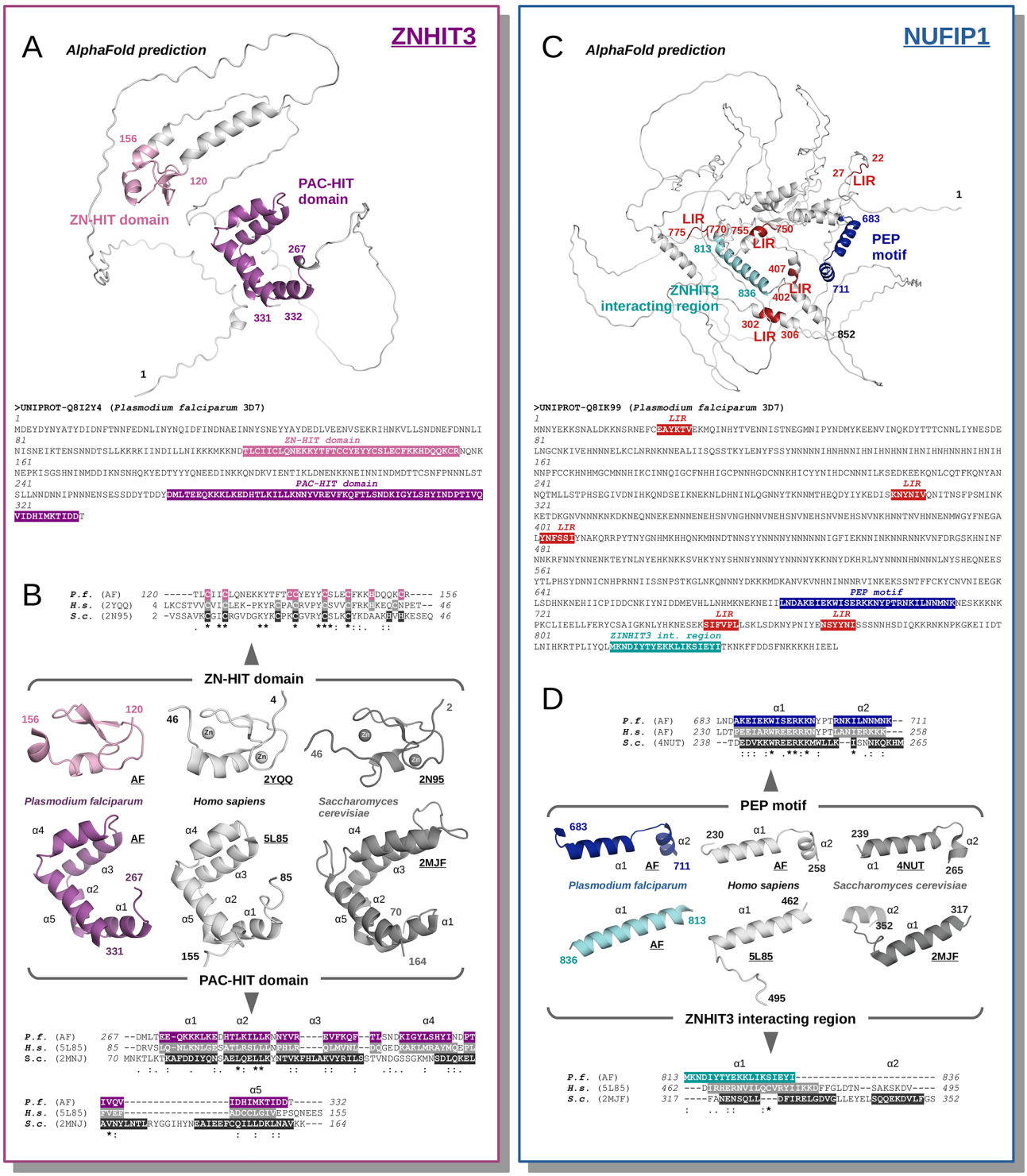

Figure 1. Structure predictions and sequence analysis of the putative proteins ZNHIT3 and NUFIP1 from *P. falciparum*. (A,C) AlphaFold 3D predictions of the Uniprot entries Q8I2Y4 (A) and Q8IK99 (C) are represented in a cartoon mode. Putative domains and interaction regions are highlighted with color on the structures and on the protein sequences. Limits of ZN-HIT and PAC-HIT domains, as well as of the LIR, PEP, and ZNHIT3 interaction regions, are indicated on the protein sequence and on the 3D structures. (B,D) Structural and sequence comparison of putative domains and interaction regions in Uniprot entries Q8I2Y4 (B) and Q8IK99 (D) with known 3D structures of human and yeast proteins ZNHIT3 (Hit1) and NUFIP1 (Rsa1). The 4-letter PDB code is indicated next to each structure, AF referring to AlphaFold predictions. Concerning the ZN-HIT domains (B), conserved cysteine and histidine residues are highlighted with color on the protein sequences. Zinc atoms are designated as Zn using a sphere representation. Concerning the PAC-HIT domains, PEP motifs, and ZNHIT3 interacting regions (B,D), α- helices are numbered and highlighted with color on the protein sequences. Concerning the PEP motif in hs-NUFIP1, the AlphaFold prediction was represented as no experimental structures are available

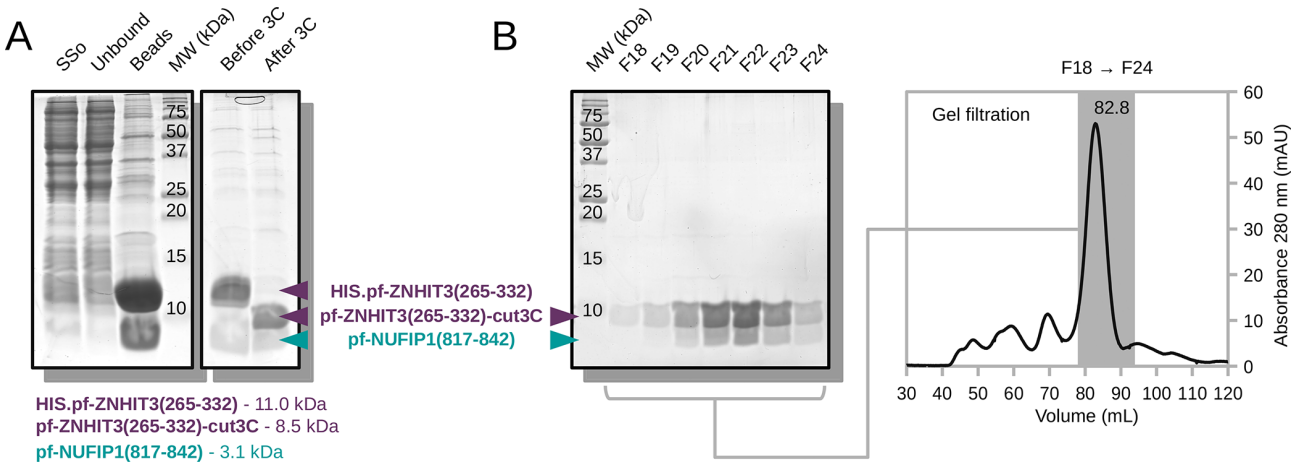

Figure 2. Purification of the plasmodial ZNHIT3(265−332)/NUFIP1(817−841) complex. (A) SDS−PAGE analysis of the affinity purification step of the co-expressed 265−332 and 817−841 fragments of pf-ZNHIT3 and pf-NUFIP1. (B) SDS−PAGE analysis and elution profile of the gel filtration step. SSo, unbound, beads, MW, 3C, and F18 to F24 refer, respectively, to the sonicate supernatant, the unbound fraction after mixture with TALON beads, the TALON beads, the protein size marker, the PreScission cleavage, and the gel filtration fractions. His-tagged and untagged protein fragments are indicated with arrows. The elution volume of the main peak observed on the gel profile is indicated.

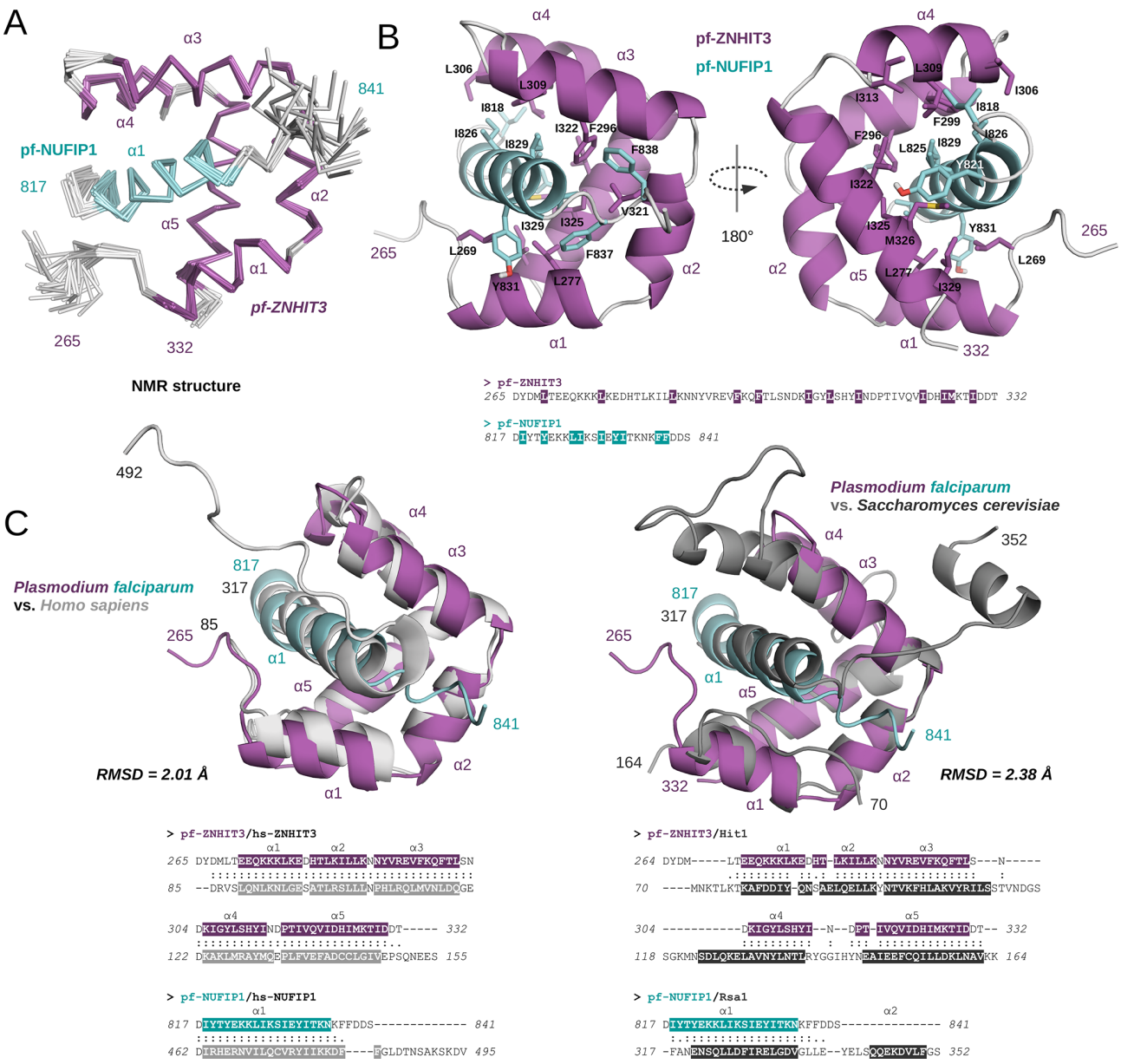

Figure 3. Structural analysis of the plasmodial ZNHIT3:NUFIP1 interaction. (A) Superimposition of the 20 best water-refined NMR structures of pf-ZNHIT3(265−332) in complex with pf-NUFIP1(817−841). N- and C-terminal amino acids are indicated, and α-helices are numbered and displayed in color. (B) Two detailed views of the hydrophobic residues involved in the protein interface. Amino acid side chains are represented with sticks, hydrogen atoms being discarded. The hydrophobic residues at the interface between pf-ZNHIT3 and pf-NUFIP1 are also highlighted in color on the protein sequences. (C) Superimposition of the 3D structures of the plasmodial and human ZNHIT3:NUFIP1 complexes (left) and of the plasmodial and yeast ZNHIT3/Hit1:NUFIP1/Rsa1 complexes. rmsd values and the structural alignment of the protein sequences computed with TM-align are reported. Limits of the α-helices are colored on the 3D structures and on the protein sequences. N- and C-terminal amino acids are indicated on the 3D structures. PDB codes for the human and yeast entries are L85 and 2MJF, respectively.

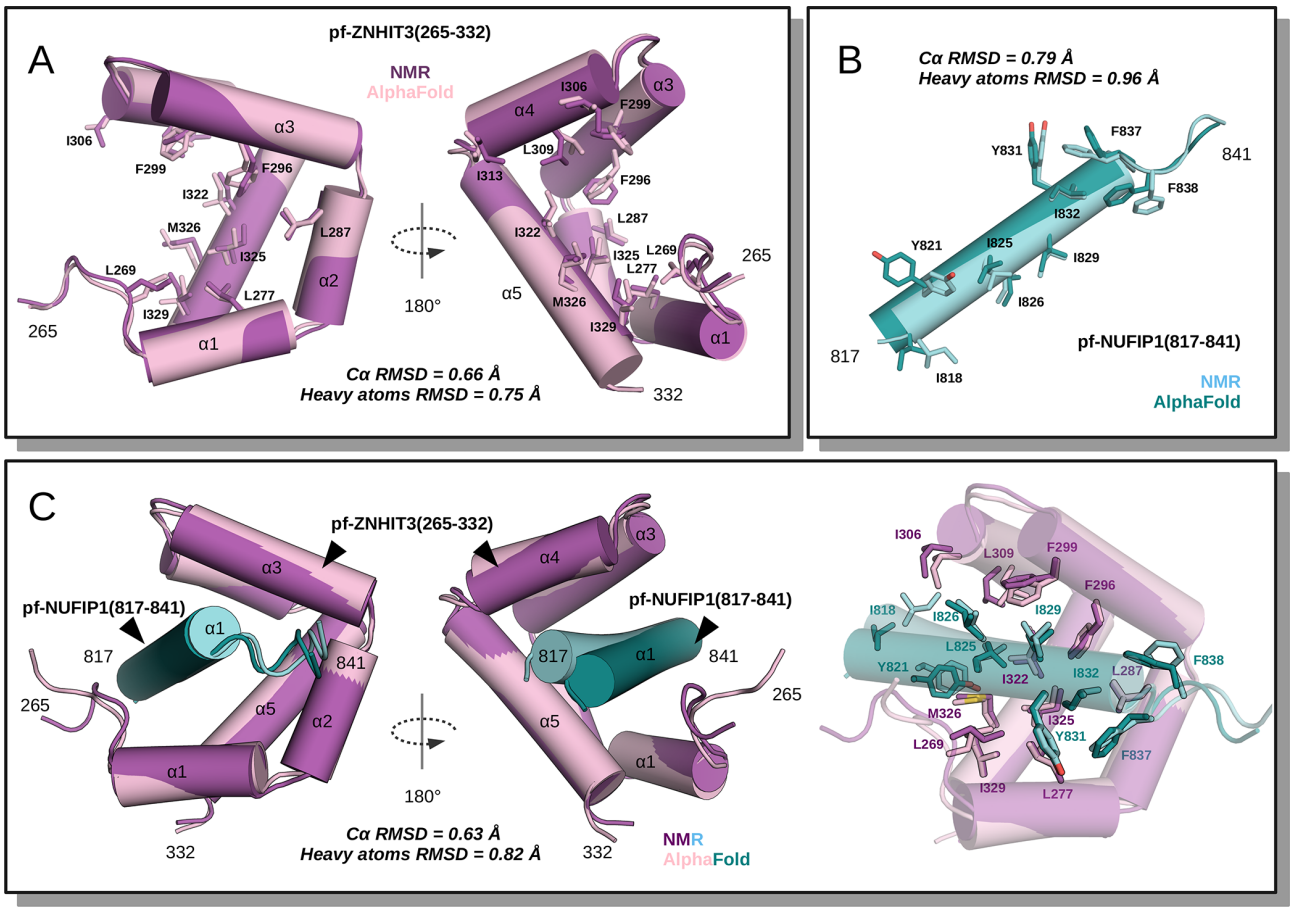

Figure 4. Comparison between the NMR and predicted 3D structures of plasmodial ZNHIT3(265−332) and NUFIP1(817−841). (A) Superimposition between the best NMR structure of pf-ZNHIT3(265−332) extracted from the structure of the complex with pf-NUFIP1(817− 841) (in magenta) and the AlphaFold prediction (in pink). (B) Superimposition between the best NMR structure of pf-NUFIP1(817−841) extracted from the structure of the complex with pf-ZNHIT3(265−332) (in cyan) and the AlphaFold prediction (in teal blue). (C) Superimposition between the best NMR structure (in magenta and cyan) and the AlphaFold prediction (in pink and teal blue) of the pf-ZNHIT3(265−332):pf-NUFIP1(817−841) complex. The hydrophobic residues located at the complex interface reported in Figure 3 are represented using sticks. The rmsd values calculated on the Cα and heavy atoms are indicated.

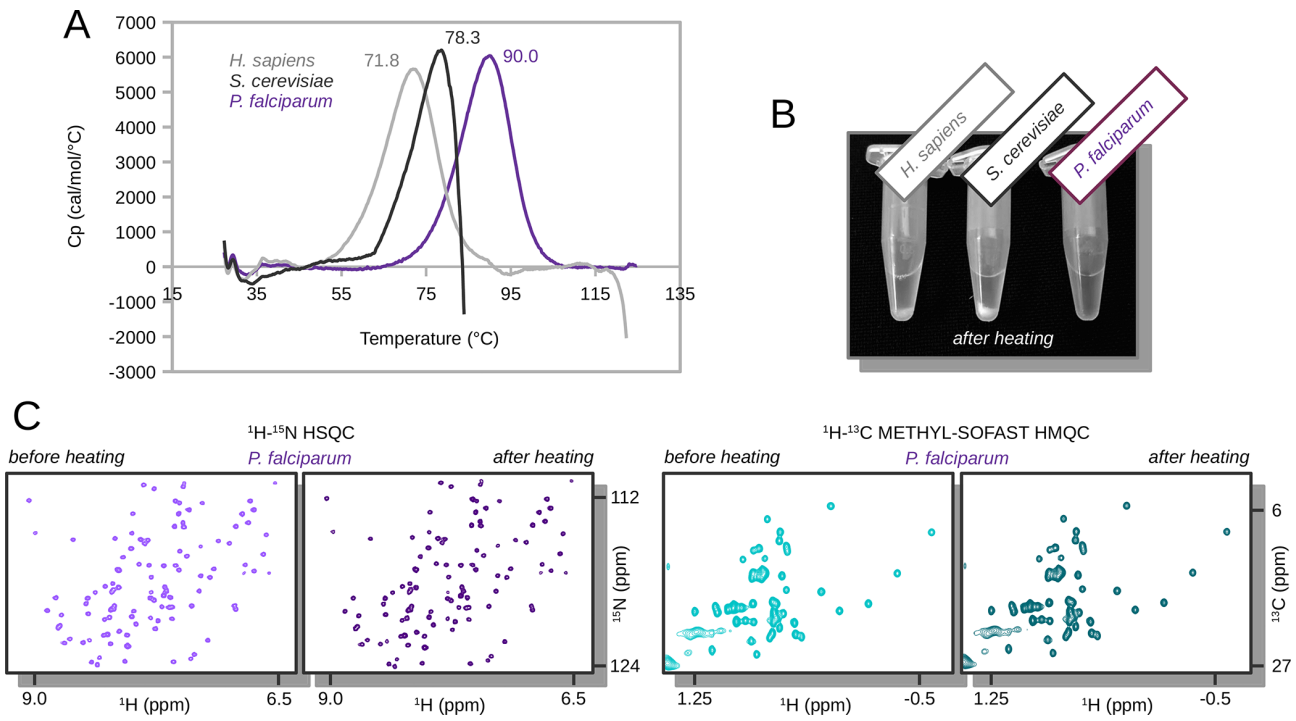

Figure 5. Thermal stability of the human, yeast, and plasmodial ZNHIT3:NUFIP1 complexes. (A) Thermograms obtained using differential scanning microcalorimetry recorded on homologue complexes hs-ZNHIT3(85−155):hs-NUFIP1(462−495) (light gray), Hit1(70−164):Rsa1- (317-352) (dark gray), and pf-ZNHIT3(265−332):pf-NUFIP1(817−841) (magenta). For each sample, the temperature midpoint of the unfolding transition (T m) is reported. C p refers to the heat capacity. (B) Picture of the sample tubes containing human, yeast, and plasmodial ZNHIT3:NUFIP1 complexes concentrated at 150 µM after heating at 98 °C, cooling at 20 °C, and centrifugation. Precipitates are visible in the first and second tubes, the third one remaining clear. (C) 1 H− 15 N HSQC and 1 H− 13 C METHYL-SOFAST HMQC spectra recorded at 20 °C on a 15 N/ 13 C-labeled sample of pf-ZNHIT3(265−332):pf-NUFIP1(817−841) concentrated at 150 µM, before and after heating at 98 °C. The spectra remain unchanged upon heating.

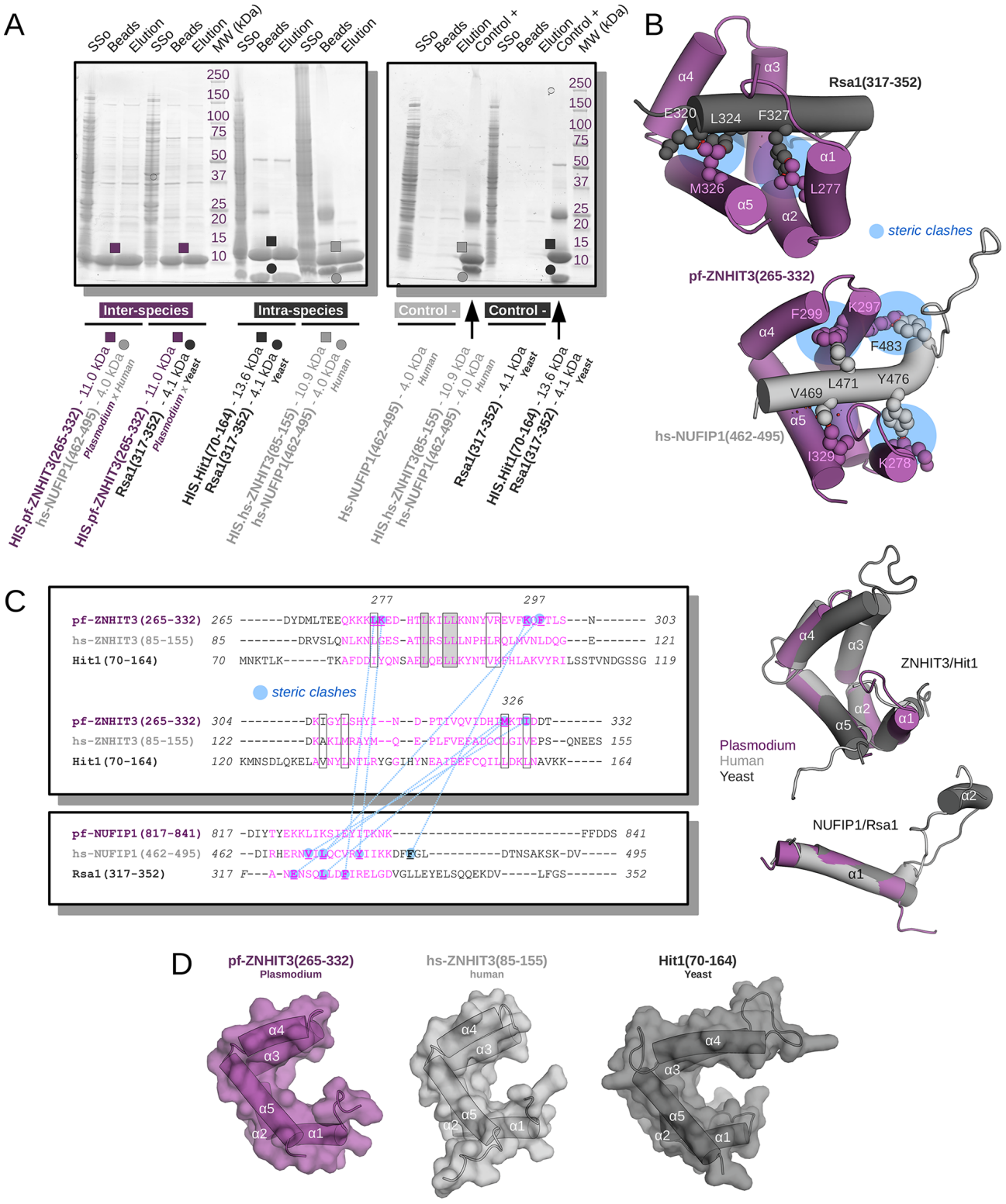

Figure 6. Inter-species protein co-expression assays. (A) SDS−PAGE analysis of pf-ZNHIT3(265−332) co-expressed with hs-NUFIP1(462−495) and Rsa1(317−352) (left part of the gel on the left). To facilitate the identification of the protein on the gel, positive controls, consisting of co- purification of the yeast and human complexes, are shown (right part of the gel on the left). Negative and positive controls done to evaluate the nonspecific binding to TALON beads of untagged human and yeast NUFIP1/Rsa1 fragments are also shown (gel on the right). ZNHIT3/Hit1 and NUFIP1/Rsa1 fragments are identified with squares and circles, respectively. SSo, Beads, Elution, and MW refer, respectively, to the sonicate supernatant, the TALON beads, the fraction eluted with imidazole, and the protein size marker. (B) Fake 3D structures of pf-ZNHIT3(265−332) in complex with hs-NUFIP1(462−495) and Rsa1(317−352). Pf-NUFIP1(817−841) was substituted by human and yeast homologue fragments, thanks to the structural alignments computed with the TM-align server displayed in Figure 3. Steric clashes occurring between amino acid side chains are highlighted in blue circles. Only non-hydrogen atoms are represented as spheres. (C) Multiple sequence alignments of the ZNHIT3/ Hit1 and NUFIP1/Rsa1 interacting regions extracted from a structural alignment performed with mTM-align. Similar and identical positions are, respectively, displayed in white and gray boxes. The pairs of residues involved in the steric clashes depicted in (B) are highlighted with blue dashed lines. The close structural superimposition between the three ZNHIT3/Hit1 and NUFIP1/Rsa1 are represented on the right. (D) Molecular surface representation of the three ZNHIT3/Hit1 structures extracted from their respective complex with NUFIP1/Rsa1.

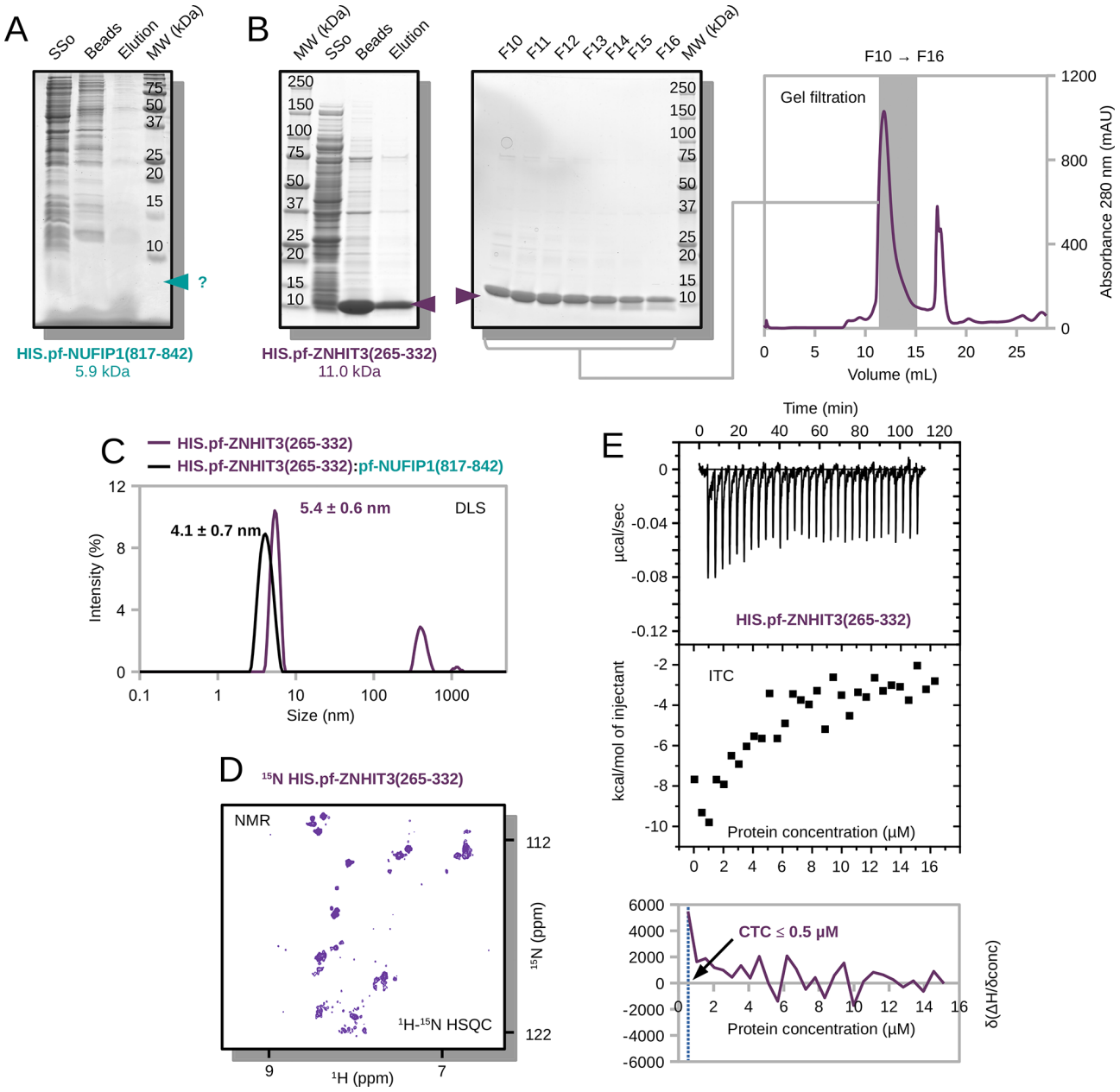

Figure 7. Biophysical analysis of the free plasmodial NUFIP1 and ZNHIT3 interacting domains. (A) SDS−PAGE analysis of the affinity purification step of the his-tagged 817−841 fragment of pf-NUFIP1. The recombinant fragment was not detected. (B) SDS−PAGE analysis and gel filtration profile of his-tagged pf-ZNHIT3(265−332). SSo, Beads, MW, Elution, and F10 to F16 refer, respectively, to the sonicate supernatant, the TALON beads, the protein size marker, the elution supernatant, and the gel filtration fractions. (C) DLS analysis of his-tagged pf-ZNHIT3(265− 332) bound or not to pf-NUFIP1(817−841). The mean protein size for the main peak is indicated. (D) 1 H− 15 N HSQC spectrum of his-tagged pf- ZNHIT3(265−332) recorded under the same conditions as the ones used for the structure determination of the complex with pf-NUFIP1(817− 841). (E) Titration isotherms of his-tagged pf-ZNHIT3(265−332) obtained upon dilution in buffer. The upper limit of CTC is indicated on the derivative curve.

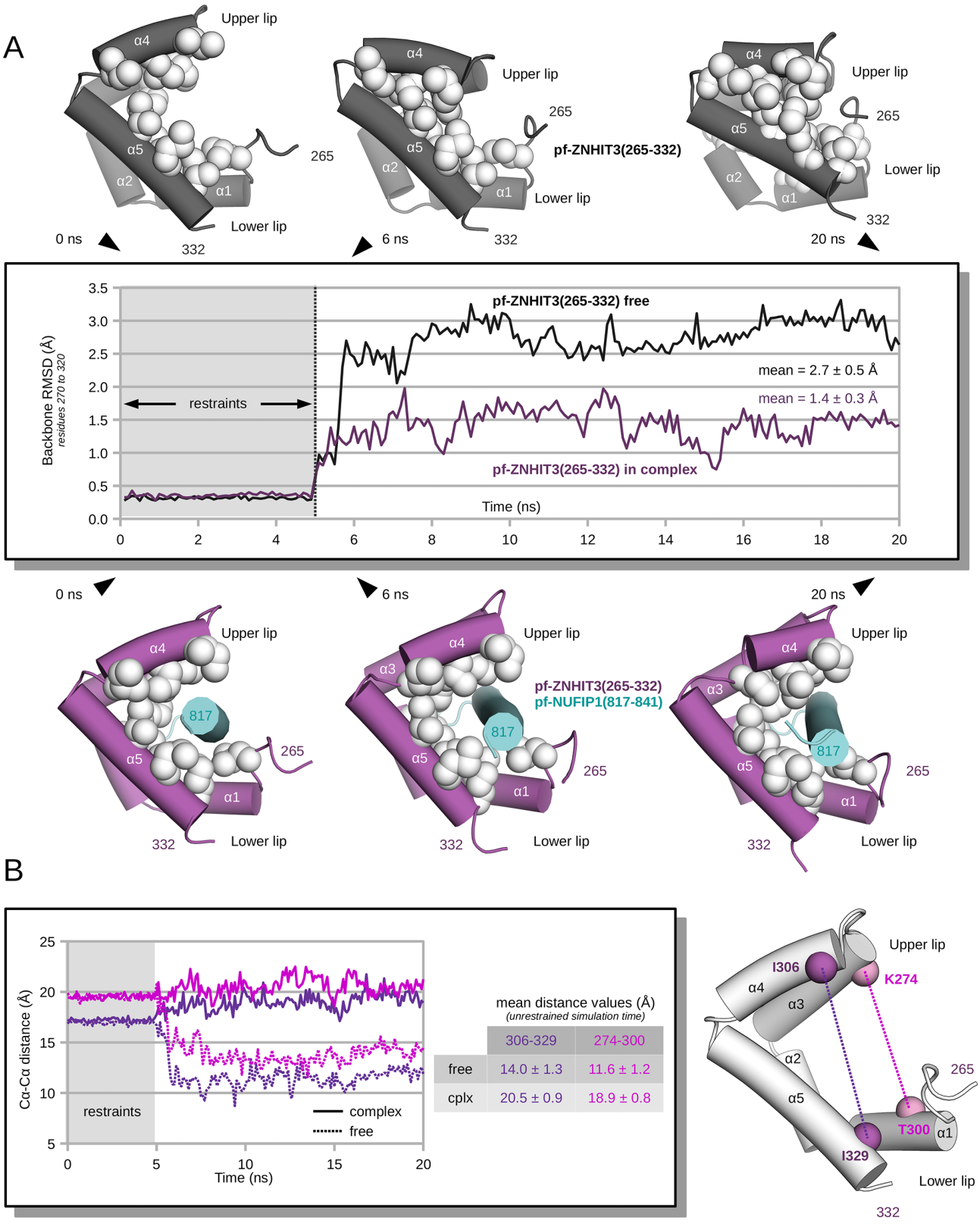

Figure 8. Analysis of the molecular dynamic simulations computed on pf-ZNHIT3(265−332) bound or not to pf-NUFIP1(817−841). (A) Evolution of the backbone rmsd value of pf-ZNHIT3(265−332) in complex with (magenta) or free of (dark gray) pf-NUFIP1(817−841) along the simulation time (residues 270−330 were considered). The 5 first ns of the trajectories, framed in light gray, corresponds to the restrained simulation time, when the positions of backbone atoms are limited. The mean values of backbone rmsd calculated during the unrestrained simulation time (meaning the last 15 ns) in these two conditions are reported. Three snapshots corresponding to the 3D structures after 0, 6, and 20 ns of simulation are displayed, respectively, on the top and the bottom of the diagram for the free and pf-NUFIP1(817−841)-bound states of pf-ZNHIT3(265−332). In these structures, the hydrophobic residues reported on the protein sequence in Figure 3 are displayed as spheres and α- helices as numbered cylinders. (B) Evolution of distances measured between Cα atoms of I306 and I329 (in magenta) and between K274 and T300 (in pink) along the simulation time. In the diagram, solid and dotted lines refer to the pf-NUFIP1(817−841)-bound and free states of pf- ZNHIT3(265−332), respectively. For each amino acid couple, the mean value of the distances calculated during the unrestrained simulation time (meaning the 15 last ns) is reported. These distances are reported on the starting 3D structure of pf-ZNHIT3(265−332), Cα atoms being represented as spheres. K274 and I306 are in the upper lip of pf-ZNHIT3(265−332) and T300 and I329 in the lower lip.

	pf-ZNHIT3(265-332):pf-NUFIP1(817-841)
NMR distances and dihedral constraints	
Total NOEs	1954
Short range ($\|i - j\| \leq 1$)	1143
Medium-range ($\|i - j\| < 5$)	475
Long-range ($\|i - j\| \geq 5$)	186
Intermolecular	150
Total dihedral angle restraints	147
Φ	74
ψ	73
Structure statistics	
Violation occurences	
Distance constraints (> 0.3 Å)	0
Dihedral angle constraints (> 5º)	0.2 ± 0.4
RMSD to best structure (Å)	
All backbone atoms	1.17 ± 0.32
All heavy atoms	1.80 ± 0.29
Backbone atoms in secondary structures	0.35 ± 0.04
Heavy atoms in secondary structures	1.01 ± 0.10
Ramachandran statistics	
Residues in most favoured regions (%)	96.2
Residues in additional allowed regions (%)	3.8
Residues in generously allowed regions (%)	0
Residues in disallowed regions (%)	0

Table 1. NMR-derived restraints and structural statistics for the 20-best water-refined structures of pf-ZNHIT3(265-332):pf-NUFIP1(817-841).

REFERENCES

(1) World Health Organization. World Malaria Report 2020: 20 Years of Global Progress and Challenges; World Health Organization:Geneva, 2020.
(2) Legrand, E.; Demar, M.; Volney, B.; Ekala, M.-T.; Quinternet, M.; Bouchier, C.; Fandeur, T.; Rogier, C.; Carme, B.; Puijalon, O. M.; Esterre, P. First Case of Emergence of Atovaquone Resistance in *Plasmodium* Falciparum during Second-Line Atovaquone-Proguanil Treatment in South America. Antimicrob. Agents Chemother. 2007, 51, 2280−2281.
(3) Sun, M.; Li, W.; Blomqvist, K.; Das, S.; Hashem, Y.; Dvorin, J. D.; Frank, J. Dynamical Features of the *Plasmodium* Falciparum Ribosome during Translation. Nucleic Acids Res. 2015, 43, gkv991−10524.
(4) Fatica, A.; Tollervey, D. Making Ribosomes. Curr. Opin. Cell Biol. 2002, 14, 313−318.
(5) Kiss, T. Small Nucleolar RNAs: An Abundant Group of Noncoding RNAs with Diverse Cellular Functions. Cell 2002, 109, 145−148.
(6) Galardi, S.; Fatica, A.; Bachi, A.; Scaloni, A.; Presutti, C.; Bozzoni, I. Purified Box C/D SnoRNPs Are Able to Reproduce Site-Specific 2'-O-Methylation of Target RNA in Vitro. Mol. Cell. Biol. 2002, 22, 6663−6668.
(7) Henras, A.; Henry, Y.; Bousquet-Antonelli, C.; Noaillac-Depeyre, J.; Gélugne, J.-P.; Caizergues-Ferrer, M. Nhp2p and Nop10p Are Essential for the Function of H/ACA SnoRNPs. EMBO J. 1998, 17, 7078−7090.
(8) Bizarro, J.; Charron, C.; Boulon, S.; Westman, B.; Pradet-Balade, B.; Vandermoere, F.; Chagot, M.-E.; Hallais, M.; Ahmad, Y.; Leonhardt, H.; Lamond, A.; Manival, X.; Branlant, C.; Charpentier, B.; Verheggen, C.; Bertrand, E. Proteomic and 3D Structure Analyses Highlight the C/D Box SnoRNP Assembly Mechanism and Its Control. J. Cell Biol. 2014, 207, 463−480.
(9) Rothé, B.; Back, R.; Quinternet, M.; Bizarro, J.; Robert, M.-C.; Blaud, M.; Romier, C.; Manival, X.; Charpentier, B.; Bertrand, E.; Branlant, C. Characterization of the Interaction between Protein Snu13p/15.5K and the Rsa1p/NUFIP Factor and Demonstration of Its Functional Importance for SnoRNP Assembly. Nucleic Acids Res. 2014, 42, 2015−2036.
(10) Rothé, B.; Saliou, J.-M.; Quinternet, M.; Back, R.; Tiotiu, D.; Jacquemin, C.; Loegler, C.; Schlotter, F.; Peñ a, V.; Eckert, K.; Moréra, S.; Dorsselaer, A. V.; Branlant, C.; Massenet, S.; Sanglier-Cianférani, S.; Manival, X.; Charpentier, B. Protein Hit1, a Novel Box C/D SnoRNP Assembly Factor, Controls Cellular Concentration of the Scaffolding Protein Rsa1 by Direct Interaction. Nucleic Acids Res. 2014, 42, 10731−10747.
(11) Pal, M.; Morgan, M.; Phelps, S. E. L.; Roe, S. M.; Parry-Morris, S.; Downs, J. A.; Polier, S.; Pearl, L. H.; Prodromou, C. Structural Basis for Phosphorylation-Dependent Recruitment of Tel2 to Hsp90 by Pih1. Structure 2014, 22, 805.
(12) Hoř ejš í, Z.; Stach, L.; Flower, T. G.; Joshi, D.; Flynn, H.; Skehel, J. M.; O'Reilly, N. J.; Ogrodowicz, R. W.; Smerdon, S. J.; Boulton, S. J. Phosphorylation-Dependent PIH1D1 Interactions Define Substrate Specificity of the R2TP Cochaperone Complex. Cell Rep. 2014, 7, 19−26.
(13) Quinternet, M.; Chagot, M.-E.; Rothé, B.; Tiotiu, D.; Charpentier, B.; Manival, X. Structural Features of the Box C/D SnoRNP Pre-Assembly Process Are Conserved through Species. Structure 2016, 24, 1693−1706.
(14) Bragantini, B.; Tiotiu, D.; Rothé, B.; Saliou, J.-M.; Marty, H.; Cianférani, S.; Charpentier, B.; Quinternet, M.; Manival, X. Functional and Structural Insights of the Zinc-Finger HIT Protein Family Members Involved in Box C/D SnoRNP Biogenesis. J. Mol.

Biol. 2016, 428, 2488−2506.
(15) Rivera-Calzada, A.; Pal, M.; Muñ oz-Hernández, H.; Luque-Ortega, J. R.; Gil-Carton, D.; Degliesposti, G.; Skehel, J. M.; Prodromou, C.; Pearl, L. H.; Llorca, O. The Structure of the R2TP Complex Defines a Platform for Recruiting Diverse Client Proteins to the HSP90 Molecular Chaperone System. Structure 2017, 25, 1145−1152.
(16) Henri, J.; Chagot, M.-E.; Bourguet, M.; Abel, Y.; Terral, G.; Maurizy, C.; Aigueperse, C.; Georgescauld, F.; Vandermoere, F.; Saint-Fort, R.; Behm-Ansmant, I.; Charpentier, B.; Pradet-Balade, B.; Verheggen, C.; Bertrand, E.; Meyer, P.; Cianférani, S.; Manival, X.; Quinternet, M. Deep Structural Analysis of RPAP3 and PIH1D1, Two Components of the HSP90 Co-Chaperone R2TP Complex. Structure 2018, 26, 1196−1209.
(17) Muñ oz-Hernández, H.; Pal, M.; Rodríguez, C. F.; Fernandez-Leiro, R.; Prodromou, C.; Pearl, L. H.; Llorca, O. Structural Mechanism for Regulation of the AAA-ATPases RUVBL1-RUVBL2 in the R2TP Co-Chaperone Revealed by Cryo-EM. Sci. Adv. 2019, 5, No. eaaw1616.
(18) Seraphim, T. V.; Chakafana, G.; Shonhai, A.; Houry, W. A. *Plasmodium* Falciparum R2TP Complex: Driver of Parasite Hsp90 Function. Biophys. Rev. 2019, 11, 1007−1015.
(19) Bragantini, B.; Charron, C.; Bourguet, M.; Paul, A.; Tiotiu, D.; Rothé, B.; Marty, H.; Terral, G.; Hessmann, S.; Decourty, L.; Chagot, M.-E.; Strub, J.-M.; Massenet, S.; Bertrand, E.; Quinternet, M.; Saveanu, C.; Cianférani, S.; Labialle, S.; Manival, X.; Charpentier, B. The Box C/D SnoRNP Assembly Factor Bcd1 Interacts with the Histone Chaperone Rtt106 and Controls Its Transcription Dependent Activity. Nat. Commun. 2021, 12, 1859.
(20) Seraphim, T. V.; Nano, N.; Cheung, Y. W. S.; Aluksanasuwan, S.; Colleti, C.; Mao, Y.-Q.; Bhandari, V.; Young, G.; Höll, L.; Phanse, S.; Gordiyenko, Y.; Southworth, D. R.; Robinson, C. V.; Thongboonkerd, V.; Gava, L. M.; Borges, J. C.; Babu, M.; Barbosa, L. R. S.; Ramos, C. H. I.; Kukura, P.; Houry, W. A. Assembly Principles of the Human R2TP Chaperone Complex Reveal the Presence of R2T and R2P Complexes. Structure 2022, 30, 156.
(21) Wyant, G. A.; Abu-Remaileh, M.; Frenkel, E. M.; Laqtom, N. N.; Dharamdasani, V.; Lewis, C. A.; Chan, S. H.; Heinze, I.; Ori, A.; Sabatini, D. M. NUFIP1 Is a Ribosome Receptor for Starvation-Induced Ribophagy. Science 2018, 360, 751−758.
(22) Heinrichs, A. Ribophagy: Selective Ribosome “Eating. Nat. Rev. Mol. Cell Biol. 2008, 9, 349.
(23) An, H.; Ordureau, A.; Körner, M.; Paulo, J. A.; Harper, J. W. Systematic Quantitative Analysis of Ribosome Inventory during Nutrient Stress. Nature 2020, 583, 303−309.
(24) Rozenknop, A.; Rogov, V. V.; Rogova, N. Y.; Löhr, F.; Gü ntert, P.; Dikic, I.; Dötsch, V. Characterization of the Interaction of GABARAPL-1 with the LIR Motif of NBR1. J. Mol. Biol. 2011, 410, 477−487.
(25) Olsvik, H. L.; Lamark, T.; Takagi, K.; Larsen, K. B.; Evjen, G.; Øvervatn, A.; Mizushima, T.; Johansen, T. FYCO1 Contains a C-Terminally Extended, LC3A/B-Preferring LC3-Interacting Region (LIR) Motif Required for Efficient Maturation of Autophagosomes during Basal Autophagy. J. Biol. Chem. 2015, 290, 29361−29374.
(26) Hain, A. U. P.; Weltzer, R. R.; Hammond, H.; Jayabalasingham, B.; Dinglasan, R. R.; Graham, D. R. M.; Colquhoun, D. R.; Coppens, I.; Bosch, J. Structural Characterization and Inhibition of the *Plasmodium* Atg8−Atg3 Interaction. J. Struct. Biol. 2012, 180, 551−562.
(27) Tomlins, A. M.; Ben-Rached, F.; Williams, R. A.; Proto, W. R.; Coppens, I.; Ruch, U.; Gilberger, T. W.; Coombs, G. H.; Mottram, J. C.; Mü ller, S.; Langsley, G. *Plasmodium* Falciparum ATG8 Implicated in Both Autophagy and Apicoplast Formation. Autophagy 2013, 9,

1540−1552.
(28) Cervantes, S.; Bunnik, E. M.; Saraf, A.; Conner, C. M.; Escalante, A.; Sardiu, M. E.; Ponts, N.; Prudhomme, J.; Florens, L.; Le Roch, K. G. The Multifunctional Autophagy Pathway in the Human Malaria Parasite, *Plasmodium* Falciparum. Autophagy 2014, 10, 80−92.
(29) Mishra, P. C.; Kumar, A.; Sharma, A. Analysis of Small Nucleolar RNAs Reveals Unique Genetic Features in Malaria Parasites. BMC Genom. 2009, 10, 68.
(30) Bateman, A.; Bateman, A.; Martin, M.-J.; Orchard, S.; Magrane, M.; Agivetova, R.; Ahmad, S.; Alpi, E.; Bowler-Barnett, E. H.; Britto, R.; Bursteinas, B.; Bye-A-Jee, H.; Coetzee, R.; Cukura, A.; Da Silva, A.; Denny, P.; Dogan, T.; Ebenezer, T.; Fan, J.; Castro, L. G.; Garmiri, P.; Georghiou, G.; Gonzales, L.; Hatton-Ellis, E.; Hussein, A.; Ignatchenko, A.; Insana, G.; Ishtiaq, R.; Jokinen, P.; Joshi, V.; Jyothi, D.; Lock, A.; Lopez, R.; Luciani, A.; Luo, J.; Lussi, Y.; MacDougall, A.; Madeira, F.; Mahmoudy, M.; Menchi, M.; Mishra, A.; Moulang, K.; Nightingale, A.; Oliveira, C. S.; Pundir, S.; Qi, G.; Raj, S.; Rice, D.; Lopez, M. R.; Saidi, R.; Sampson, J.; Sawford, T.; Speretta, E.; Turner, E.; Tyagi, N.; Vasudev, P.; Volynkin, V.; Warner, K.; Watkins, X.; Zaru, R.; Zellner, H.; Bridge, A.; Poux, S.; Redaschi, N.; Aimo, L.; Argoud-Puy, G.; Auchincloss, A.; Axelsen, K.; Bansal, P.; Baratin, D.; Blatter, M.-C.; Bolleman, J.; Boutet, E.; Breuza, L.; Casals-Casas, C.; de Castro, E.; Echioukh, K. C.; Coudert, E.; Cuche, B.; Doche, M.; Dornevil, D.; Estreicher, A.; Famiglietti, M. L.; Feuermann, M.; Gasteiger, E.; Gehant, S.; Gerritsen, V.; Gos, A.; Gruaz-Gumowski, N.; Hinz, U.; Hulo, C.; Hyka-Nouspikel, N.; Jungo, F.; Keller, G.; Kerhornou, A.; Lara, V.; Le Mercier, P.; Lieberherr, D.; Lombardot, T.; Martin, X.; Masson, P.; Morgat, A.; Neto, T. B.; Paesano, S.; Pedruzzi, I.; Pilbout, S.; Pourcel, L.; Pozzato, M.; Pruess, M.; Rivoire, C.; Sigrist, C.; Sonesson, K.; Stutz, A.; Sundaram, S.; Tognolli, M.; Verbregue, L.; Wu, C. H.; Arighi, C. N.; Arminski, L.; Chen, C.; Chen, Y.; Garavelli, J. S.; Huang, H.; Laiho, K.; McGarvey, P.; Natale, D. A.; Ross, K.; Vinayaka, C. R.; Wang, Q.; Wang, Y.; Yeh, L.-S.; Zhang, J.; Ruch, P.; Teodoro, D.; The UniProt Consortium. UniProt: The Universal Protein Knowledgebase in 2021. Nucleic Acids Res. 2021, 49, D480−D489.
(31) Diebold, M. L.; Fribourg, S.; Koch, M.; Metzger, T.; Romier, C. Deciphering Correct Strategies for Multiprotein Complex Assembly by Co-Expression: Application to Complexes as Large as the Histone Octamer. J. Struct. Biol. 2011, 175, 178.
(32) Keller, R. L. J. Computer-Aided Resonance Assignment Tutorial, 1st ed.; CANTINA Verlag: Zü rich, 2004.
(33) Shen, Y.; Bax, A. Protein Backbone and Sidechain Torsion Angles Predicted from NMR Chemical Shifts Using Artificial Neural Networks. J. Biomol. NMR 2013, 56, 227−241.
(34) Gü ntert, P. Automated NMR Structure Calculation with CYANA. Methods Mol. Biol. 2004, 278, 353−78.
(35) Case, D. A.; Cheatham, T. E.; Darden, T.; Gohlke, H.; Luo, R.; Merz, K. M.; Onufriev, A.; Simmerling, C.; Wang, B.; Woods, R. J. The Amber Biomolecular Simulation Programs. J. Comput. Chem. 2005, 26, 1668−1688.
(36) Schrödinger, L. L. C. The PyMOL Molecular Graphics System, version 1.8, 2015.
(37) Barranco-Medina, S.; Kakorin, S.; Lázaro, J. J.; Dietz, K.-J. Thermodynamics of the Dimer−Decamer Transition of Reduced Human and Plant 2-Cys Peroxiredoxin. Biochemistry 2008, 47, 7196−7204.
(38) Carrasco, K.; Boufenzer, A.; Jolly, L.; Le Cordier, H.; Wang, G.; Heck, A. J.; Cerwenka, A.; Vinolo, E.; Nazabal, A.; Kriznik, A.; Launay, P.; Gibot, S.; Derive, M. TREM-1 Multimerization Is Essential for Its Activation on Monocytes and Neutrophils. Cell. Mol. Immunol. 2019, 16, 460−472.

(39) Chagot, M.-E.; Morais, R. D. S.; Dermouche, S.; Lefebvre, D.; Manival, X.; Chipot, C.; Dehez, F.; Quinternet, M. Binding Properties of the Quaternary Assembly Protein SPAG1. Biochem. J. 2019, 476, 1679−1694.
(40) Humphrey, W.; Dalke, A.; Schulten, K. VMD: Visual Molecular Dynamics. J. Mol. Graph. 1996, 14, 33−38.
(41) Phillips, J. C.; Braun, R.; Wang, W.; Gumbart, J.; Tajkhorshid, E.; Villa, E.; Chipot, C.; Skeel, R. D.; Kalé, L.; Schulten, K. Scalable Molecular Dynamics with NAMD. J. Comput. Chem. 2005, 26, 1781−1802.
(42) Jumper, J.; Evans, R.; Pritzel, A.; Green, T.; Figurnov, M.; Ronneberger, O.; Tunyasuvunakool, K.; Bates, R.; Zˇídek, A.; Potapenko, A.; Bridgland, A.; Meyer, C.; Kohl, S. A. A.; Ballard, A. J.; Cowie, A.; Romera-Paredes, B.; Nikolov, S.; Jain, R.; Adler, J.; Back, T.; Petersen, S.; Reiman, D.; Clancy, E.; Zielinski, M.; Steinegger, M.; Pacholska, M.; Berghammer, T.; Bodenstein, S.; Silver, D.; Vinyals, O.; Senior, A. W.; Kavukcuoglu, K.; Kohli, P.; Hassabis, D. Highly Accurate Protein Structure Prediction with AlphaFold. Nature 2021, 596, 583−589.
(43) Jacomin, A.-C.; Samavedam, S.; Promponas, V.; Nezis, I. P. ILIR Database: A Web Resource for LIR Motif-Containing Proteins in Eukaryotes. Autophagy 2016, 12, 1945−1953.
(44) Zhang, Y.; Skolnick, J. TM-Align: A Protein Structure Alignment Algorithm Based on the TM-Score. Nucleic Acids Res. 2005, 33, 2302−2309.
(45) Dong, R.; Pan, S.; Peng, Z.; Zhang, Y.; Yang, J. MTM-Align: A Server for Fast Protein Structure Database Search and Multiple Protein Structure Alignment. Nucleic Acids Res. 2018, 46, W380.